


Coherent Free-Space Optical Communications: Opportunities and Challenges

Fernando P. Guiomar , Marco A. Fernandes , J. Leonardo Nascimento, Vera Rodrigues ,
and Paulo P. Monteiro 

(Invited Paper)

Abstract—The ever-increasing data rate demand for wireless systems is pushing the physical limits of standalone radio-frequency communications, thus fostering the blooming of novel high-capacity optical wireless solutions. This imminent penetration of optical communication technologies into the wireless domain opens up a set of novel opportunities for the development of a new generation of wireless systems providing unprecedented capacity. Unlocking the full potential of free-space optics (FSO) transmission can only be achieved through a seamless convergence between the optical fiber and optical wireless domains. This will allow taking advantage of the staggering progress that has been made on fiber-based communications during the last decades, namely leveraging on the latest generation of Terabit-capable coherent optical transceivers. On the other hand, the development of these high-capacity optical wireless systems still faces a set of critical challenges, namely regarding the impact of atmospheric turbulence and pointing errors. In this work, we provide an in-depth experimental analysis of the main potentialities and criticalities associated with the development of ultra-high-capacity FSO communications, ultimately leading to the long-term (48-hours) demonstration of a coherent FSO transmission system delivering more than 800 Gbps over ~42 m link length, in an outdoor deployment exposed to time-varying turbulence and meteorological conditions.

Index Terms—Free-space optics, coherent optics, adaptive modulation, optical beam steering.

I. INTRODUCTION

WIRELESS transmission is a key underlying technology for modern telecommunication systems, playing a crucial role in enabling generalized access to high-speed communications [1]. Traditionally, wireless systems are tightly associated with radio-frequency (RF) communications, owing

This work was partially supported by the European Regional Development Fund (FEDER), through the Regional Operational Programme of Centre (CENTRO 2020) of the Portugal 2020 framework, through projects ORCIP (CENTRO-01-0145-FEDER-022141) and SOCA (CENTRO-01-0145-FEDER-000010), by FCT/MCTES through projects FreeComm-B5G (UIDB/EEA/50008/2020), LandMark (POCI-01-0145-FEDER-031527), OptWire (PTDC/EEI-TEL/2697/2021) and CESAM financial support (UIDP/50017/2020 + UIDB/50017/2020 + LA/P/0094/2020) and by the MSCA RISE programme through project DIOR (grant agreement no. 10100828). Fernando P. Guiomar acknowledges a fellowship from “la Caixa” Foundation (ID 100010434), code LCF/BQ/PR20/11770015. Marco A. Fernandes acknowledges a PhD fellowship from FCT, code 2020.07521.BD.

Fernando P. Guiomar, Marco A. Fernandes, José L. Nascimento and Paulo P. Monteiro are with Instituto de Telecomunicações, University of Aveiro, 3810-193, Aveiro, Portugal (e-mail: guiomar@av.it.pt)

Vera Rodrigues is with CESAM & Department of Environment and Planning, University of Aveiro, 3810-193, Aveiro, Portugal (e-mail: vera.rodrigues@ua.pt)

Manuscript received December XX, 2021; revised December XX, 2021.

to decades of impressive developments and commercial deployment, which have put RF-based technologies at the core of wireless access. However, the eminent upsurge of increasingly bandwidth-hungry applications might become a major game-changer in the near future [2], [3].

Notably, this upcoming bandwidth bottleneck is already being addressed in the discussion of next generation cellular communications – the 6th-generation (6G) – where the auxiliary use of optical wireless communications (OWC) is being considered for the first time [3]. Typically, OWC is a general designation that encompasses multiple technologies, spanning over a wide range of wavelengths, from the near-infrared to the ultraviolet spectrum [4]. Particularly, the use of wavelengths in the range of 1300–1600 nm – where OWC becomes more commonly defined as free-space optics (FSO) communication [5] – is currently attracting significant interest, benefiting from their compatibility with fiber-based transmission, thereby enabling the seamless convergence between high-capacity wired and wireless domains [6].

Owing to their inherent high-capacity and high-directivity, FSO communications are prone to find practical application not only in the access sector but also in the transport and core sections of the network, where both higher transmission distances and data rates must be simultaneously supported. The use case of inter-satellite [18] and satellite-to-earth communications [19] provides a prominent example of the successful exploitation of the distinctive features of FSO systems for space communications [20]. Another uprising application scenario arises in the context of data center networks (DCN) [21], either for inter-rack or inter-cluster communications [22], [23], instigated by the need to reduce transmission latency as well as the density and complexity of wired connections within the data center [24].

While current commercial FSO systems still operate with simple intensity modulation and direct detection (IMDD), enabling per-channel data rates in the range of 1–10 Gbps [25], the demand for higher data rates is quickly driving the research community into finding novel high-capacity FSO solutions. In this regard, a key step forward is to avoid the bandwidth bottleneck imposed by optical-to-electrical (O/E) endpoints of an FSO link. Alternatively, by employing direct air-to-fiber optical signal coupling using collimation lenses, a seamless convergence between the fiber-based network and the wireless link is achieved [26], thereby preserving the enormous bandwidth provided by the optical fiber. The direct collimation of the optical signal into the fiber core

TABLE I
SUMMARY OF HIGH-CAPACITY FSO FIELD DEMONSTRATIONS

| reference | year | bit-rate | # channels | modulation format | spectral efficiency | link length | receiver |
|-----------|------|------------|------------|-------------------|---------------------|-------------|--------------------|
| [7] | 2003 | 80 Gbps | 8 | OOK | 0.1 b/s/Hz | 3.4 km | direct detection |
| [8] | 2008 | 160 Gbps | 16 | OOK | 0.1 b/s/Hz | 2.16 km | direct detection |
| [9] | 2009 | 1.28 Tbps | 32 | OOK | 0.4 b/s/Hz | 212 m | direct detection |
| [10] | 2013 | 1.6 Tbps | 16 | QPSK | 1 b/s/Hz | 80 m | coherent detection |
| [11] | 2018 | 120 Gbps | 3 | QPSK | 0.5 b/s/Hz | 1 km | coherent detection |
| [12] | 2019 | 13.16 Tbps | 54 | QPSK | 4.9 b/s/Hz | 10.45 km | coherent detection |
| [13] | 2020 | 448 Gbps | 4 | PAM4 | 0.3 b/s/Hz | 600 m | direct detection |
| [14] | 2020 | 200 Gbps | 2 | 32QAM | 4 b/s/Hz | 55 m | direct detection |
| [15] | 2020 | 400 Gbps | 1 | PCS-64QAM | 6 b/s/Hz | 55 m | coherent detection |
| [16] | 2021 | 14 Tbps | 35 | PCS-16QAM | 4 b/s/Hz | 220 m | coherent detection |
| [17] | 2021 | 800 Gbps | 16 | PAM4 | 0.5 b/s/Hz | 200 m | direct detection |
| this work | 2022 | 800 Gbps | 1 | PCS-64QAM | 8.5 b/s/Hz | 42 m | coherent detection |

also provides an embedded support to wavelength-division multiplexing (WDM) transmission over the free-space link, thereby enabling successive FSO transmission experiments with record-high bit-rates. A summary of some of the highest-capacity FSO outdoor demonstrations is provided in Table I.

This also facilitates the adoption of state-of-the-art high-capacity optical fiber transceivers for FSO applications [12]. Particularly, the use of coherent optical communications together with advanced modulation formats and digital signal processing [27] is a promising approach that is recently standing out, enabling FSO communications at unprecedented per-channel data rates of up to 1 Tbps [28], [29] and aggregated multichannel data rates of more than 14 Tb/s [16], employing wavelength-division multiplexing (WDM). Noteworthy, besides the plethora of recent research-oriented works, coherent FSO systems are already finding their first commercial applications in the rapidly expanding space sector. A notable example is given by NASA's Terabyte Infrared Delivery (TBird) program, which is developing 200 Gbps satellite-to-earth optical links resorting to the adaption of C form-factor pluggable (CFP) coherent fiber transceivers [30].

Despite the ultra-high capacity enabled by FSO, its widespread commercial adoption still faces a handful of critical challenges, mainly in terms of communication reliability. Among these, the two major technical issues that span across most FSO applications are i) the impact of atmospheric turbulence [31], [32] and ii) the tight requirements on optical beam alignment [33], [34]. Atmospheric turbulence is a key distinguishing feature of FSO channels: unlike fiber-based systems, the received optical signal suffers from random power fluctuations, a phenomenon that is commonly denominated as optical scintillation [35]. To capture this effect, several statistical models have been proposed and validated in the last decades, namely the log-normal [36] and Gamma-Gamma [37] models, which are adequate for weak and strong turbulence regimes, respectively. Although sometimes overlooked, a prominent feature of these systems lies in the coherence time of the atmospheric channel [38] (typically in the range of 10 μ s–10 ms [39]), which opens up the possibility to develop effective FSO channel estimation techniques [40]–[42], thereby enabling to track and partially compensate for the scintillation effect [15], [42]. On what concerns optical beam alignment, it is well-known that

FSO systems with direct air-to-fiber coupling are particularly sensitive to the angle-of-arrival (AoA) of the optical signal [26], thereby tightening the precision required for the beam alignment task. To that end, several acquisition, tracking and pointing (ATP) mechanisms have been recently proposed [43], which can be broadly categorized into mechanical (e.g. gimbal-based and/or mirror-based), electromechanical (e.g. deformable mirrors) and electrical (e.g. liquid crystals) approaches. While electrical and electromechanical techniques provide the highest beam-steering precision (nrad resolution), mechanical systems are typically required to ensure a wide-enough field-of-view, together with μ rad steering resolution, which might be sufficient for most short and medium-reach (<10 km) FSO applications [44]. To that end, gimbal-based systems have been widely exploited in the literature, either operating with standalone optical beam alignment control [44] or with an auxiliary O/E mechanism, such as a quadrant detector [45], spatial light modulator [17] or near-infrared camera [46]. In these systems, the digital control algorithm plays a key role in finding and keeping the optimum alignment between transmitter and receiver. Given the complexity of this task, the use of artificial intelligence (AI) has been recently demonstrated to provide improved system reliability [44]. A particularly promising optical beam steering technique composed of a pair of fast steering mirrors, infrared LEDs and cameras is demonstrated in [47], allowing a wide field-of-view of 50° with a tracking accuracy of 0.02° and 200 ms latency.

Following our previous conference paper [27], in this work we provide an in-depth experimental overview on the practically achievable performance of coherent FSO systems, thereby opening an outlook into the opportunities and criticalities of this technology. Throughout the following sections, we will explore the dichotomy between achievable capacity and reliability, experimentally addressing and proposing mitigation solutions for the two key challenges discussed above: atmospheric turbulence and optical beam alignment. Besides the general overview of the latest developments on coherent FSO systems, in this work we provide the following main novel contributions:

- i) *optical beam steering*: we perform a complete analysis of the optical beam alignment requirements of coherent FSO systems with direct collimation of the wireless signal into the fiber core, and a direct comparison against

low-bandwidth (15 MHz) and high-bandwidth (15 GHz) free-space photodiode receivers typically used in IMDD systems;

- ii) *atmospheric turbulence modeling*: we carry out a dedicated experimental campaign with week-long measurements over a 42 m long outdoor FSO link, providing a detailed analysis of atmospheric turbulence effects. A simple methodology is proposed to properly isolate slow fading and turbulence-induced fading effects, thereby enabling an accurate modeling of optical scintillation using a Gamma-Gamma theoretical reference.
- iii) *FSO channel estimation*: we propose novel algorithms based on least-mean squares (LMS) and recursive least squares (RLS) adaptive filters, which are shown to provide improved performance over the simpler moving average filter proposed in [15];
- iv) *high-capacity coherent FSO transmission*: a novel 48-hours experimental campaign is carried out to demonstrate for the first time 800G+ transmission over a single optical channel in realistic outdoor conditions. The potential gains in turbulence mitigation enabled an optical pre-amplifier with automatic gain control are also experimentally assessed.

All collected data sets utilized in this paper are made available through an open-source repository [48].

The remainder of this paper is structured as follows: in section II we discuss the main challenges and potential solutions for optical beam steering in all-optical coherent FSO links, providing a direct comparison against O/E-based receivers. Then, in section III, we proceed with the experimental and numerical modeling of the FSO channel, focusing on the independent treatment of slow and fast optical power variations, and leading to the optimized design of channel estimation tools. Benefiting from these findings, in section IV we experimentally demonstrate the long-term operation of an 800G+ coherent FSO system, addressing the mitigation of channel-induced losses through a gain-controlled pre-amplified receiver. Finally, the main conclusions are drawn in section V.

II. OPTICAL BEAM STEERING: REQUIREMENTS AND SOLUTIONS

Let us start by tackling the issue of optical beam steering in coherent FSO systems, considering two complementary perspectives. First, we will experimentally characterize the requirements in terms of alignment precision, comparing different receiver typologies. Then, we will demonstrate an AI-assisted adaptive beam alignment technique that is able to blindly converge the optimum alignment point.

A. Characterization of Optical Beam Alignment Requirements

In this section, we experimentally characterize the optical beam alignment requirements of a 3 m-long FSO link¹

¹Note that the FSO link length (3 m) adopted in this part of the work is basically limited by the space constraints of our laboratory. Therefore, it is worth emphasizing that, in a practical deployment, the actual optical beam steering requirements will strongly depend on the geometry of the link.

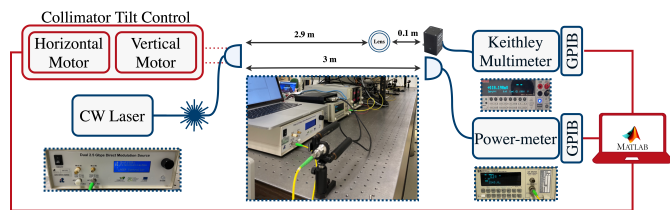


Fig. 1. Indoor experimental setup for the implementation of optical beam steering with different FSO receiver typologies.

resorting to the laboratory setup shown in Fig. 1. The optical source derives from a continuous wave (CW) laser emitting a 5 dBm beam at 1550 nm, which is connected to a Thorlabs F810APC-1550 fiber collimator with 24 mm diameter, 0.00017° divergence angle, 0.24 numerical aperture, and 37.13 mm focal length. The collimator holder is equipped with two stepper motorized actuators (Thorlabs ZST206) that control the transmitting collimator's tilt, allowing the beam alignment to be managed via MATLAB.

Two different receiver typologies were explored: i) an O/E-based receiver, implemented by an unamplified photodetector (Newport 818-BB-35 InGaAs PIN), and ii) a direct air-to-fiber coupling receiver, implemented by a fiber collimator (Thorlabs F810APC-1550, equal to the transmitter). In the O/E-based receiver, the photodetector is characterized by a 0.032 mm active area diameter, a working wavelength range of 1000–1650 nm, and < 25 ps rise time (~15 GHz bandwidth). The usage of a high-speed photodetector implied the utilization of a plano-convex optical lens (Thorlabs LA5817) to decrease the transmitted beam diameter, with the output voltage being measured by a Keithley 2004C SourceMeter. In contrast, the direct air-to-fiber receiver only requires an additional power meter (HP-8157A) to measure the received optical power. The MATLAB script uses a grid-search-like algorithm to drive the stepper motors that control the transmitting collimator, sweeping the receiver aperture while registering the respective optical-power/voltage measurements.

Figure 2 represents a three-dimensional depiction of the normalized characterization measurements as a function of beam displacement for both the collimator (solid representation) and the photodetector with lens (contour lines). The results show an extremely acute sensitivity on both the fiber collimator and the O/E-based receiver, requiring sub-mm precision to avoid high induced losses. Figure 3 illustrates a horizontal section cut of the normalized characterization measurements, including an additional low-bandwidth (~15 MHz) photodetector (Thorlabs SM05PD5A with Thorlabs LA5817), with each marker denoting a loss of 3 dB in received power. From the obtained results, it is possible to assess that both the high-speed photodetector (Newport 818-BB-35 InGaAs PIN) and collimator-based systems demonstrate similar behavior for up to 1 mm misalignment tolerance at the receiver, yielding approximately 20 dB loss on the received optical power, which represents the region of interest for most FSO communications; i.e. higher misalignment would lead to excessive SNR loss that may render the system unpractical for high-speed communications.

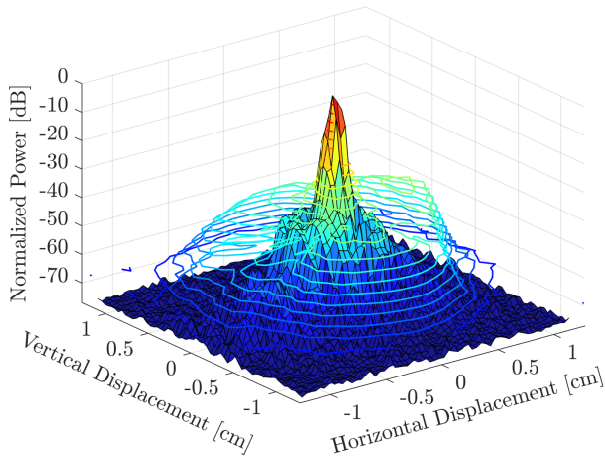


Fig. 2. Characterization of normalized received optical power as a function of vertical and horizontal displacement of the FSO receiver. Solid surface: normalized received power from the direct air-to-fiber receiver using Thorlabs F810APC fiber collimator. Countour lines: normalized received power from O/E-based receiver using Newport 818-BB-35 photodetector and Thorlabs LA5817 lens.

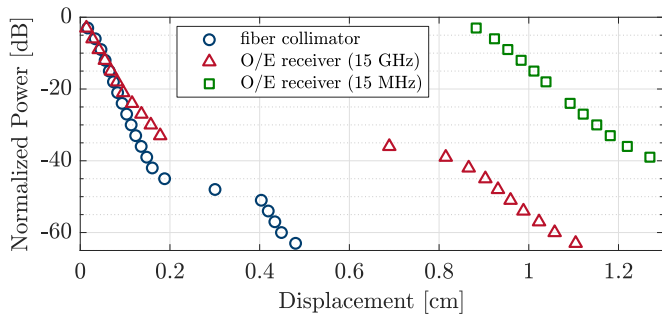


Fig. 3. Characterization of horizontal displacement tolerance measured with the Thorlabs F810APC-1550 fiber collimator and two different O/E receivers: i) a wideband (15 GHz) Newport 818-BB-35 InGaAs photodetector and ii) a narrowband (15 MHz) Thorlabs SM05PD5A InGaAs photodetector. The O/E receivers are aided by an additional focusing lens, Thorlabs LA5817.

In contrast, the low-bandwidth photodetector (Thorlabs SM05PD5A) shows a significantly improved tolerance to beam misalignment, allowing for an offset of more than 1 cm at 20 dB loss.

Fundamentally, these results expose the well-known tradeoff between bandwidth and active area associated with free-space photodetectors: a high bandwidth requires a low capacitance of the P-N junction, which in turn restricts the maximum size of the photodiode's active area. This intrinsic limitation makes the optical beam alignment in O/E-based receivers more and more challenging as bandwidth increases. A potential solution to circumvent this limitation lies in the development of photodetector arrays [49], [50], allowing to extend the bandwidth-vs-size tradeoff at the expense of additional hardware and a proportional increase of power consumption and cost.

In turn, the use of direct air-to-fiber coupling using optical collimation lenses is primarily dictated by the size of the focusing lens and the effective core area of the optical fiber at the receiver. It is important to emphasize that the mm-range

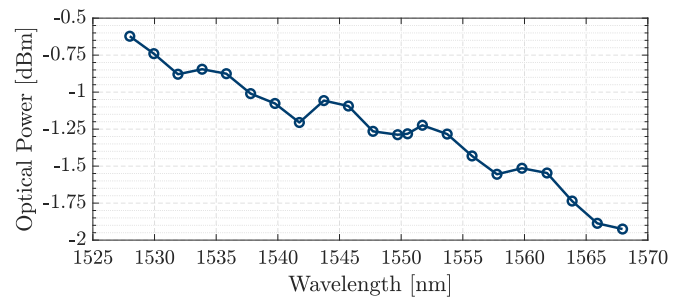


Fig. 4. Received optical power fluctuations per wavelength on a 3 m FSO link utilizing optical fiber collimators at the transmitter and receiver ends.

beam steering requirements derived from Fig. 3 are tied to the considered geometry of the FSO link (3 m long, with 2.4 cm receiver lens). In general, for simple trigonometric reasons, the angular resolution required for beam steering becomes increasingly more stringent as the link distance increases. On the other hand, the usage of wider area optical telescopes, or different receiver architectures (see e.g. [47], [51]), can allow to significantly relax the beam steering requirements. In order to enhance the alignment tolerance, the use of large area few-mode fibers has also been recently proposed [52]–[54], enabling significantly enhanced robustness not only towards pointing errors but also regarding turbulence-induced scintillation [52]. However, the use of few-mode fibers at the receiver end still imposes a significant increase on the receiver complexity, namely requiring an additional component for mode-demultiplexing and a dedicated coherent receiver for each received mode. In that regard, and despite tightening the optical beam alignment requirements, the use of standard single-mode fibers still provides the best compatibility with current fiber-based coherent receivers. In any case, and in contrast with O/E-based receivers, the use of direct air-to-fiber coupling inherently ensures an enormous operation bandwidth where the optical beam alignment requirements are approximately fixed. In order to better illustrate this feature, in Fig. 4 we show the dependence of received optical power on the wavelength of the transmitted signal.

After preliminary optical beam alignment for the central wavelength (1550 nm), we swept the wavelength of the transmitting laser within the C-band and registered the corresponding received optical power without further alignment. The transmitted optical power was also monitored to ensure a stable output level. The obtained results show that the utilized optical fiber collimators enable to seamlessly stream the optical signal over the air within the full C-band (typically used in fiber-based telecommunications) with a maximum differential loss of approximately 1.5 dB. In comparison to the tested 15 GHz O/E-based receiver, this corresponds to a staggering ~ 5 THz operating bandwidth, thus effectively providing a future-proof solution for high-capacity FSO communications.

B. Adaptive Beam Steering Algorithms

The experimental characterization presented in the previous section serves the purpose of establishing the requirements

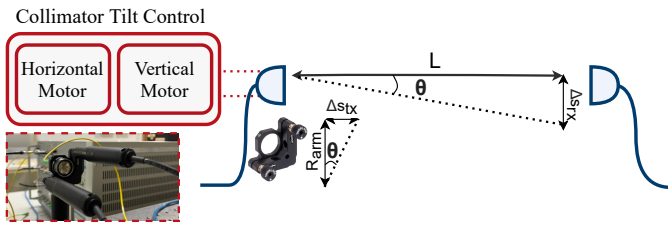


Fig. 5. Schematic representation of a gimbal-based ATP mechanism and the respective precision requirements for the motorized actuators.

for the design of an ATP system implementing automatic beam alignment. From the plethora of different ATP options, gimbal-based alignment stands out due to its low-complexity and low-cost allied to a wide field of view. However, gimbal-based ATP systems come with limited precision when compared with other systems like adaptive optics. This advantage is partially mitigated by the recent advances in high-precision motion controllers, including stepper motors and piezoelectric actuators. As shown in the previous section, satisfactory optical beam steering requires sub-mm precision at the receiver, Δs_{rx} , where Δs_{rx} represents the minimum translation of the received beam spot over the plane defined by the receiving collimator lens. However, in a gimbal-based ATP system, this incremental movement of the beam spot at the receiver plane is obtained by controlling the tilt of the transmitting collimator. Typically, the transmitting collimator is installed on a precision kinematic mount, which provides two adjusting axes to control the vertical and horizontal tilt of the mounted collimator. The tilt of the collimator mount can then be controlled through the linear motion, Δs_{tx} , of the leadscrew of a couple of high-precision motion actuators. This implementation is illustrated in the block diagram of Fig.5, where for simplicity only the vertical tilt axis at the transmitter is represented. Let us also consider that the receiver collimator has been already angularly aligned with the transmitter, thus avoiding the impact of AoA mismatch between the transmitting and receiving ends, in which case beam wandering is only caused by transmitter pointing errors into the receiver lens.² Under this simplified assumption, the required precision for the linear motion of the actuator's leadscrew can be calculated as,

$$\Delta s_{tx} = \frac{\Delta s_{rx}}{L} \times R_{arm}, \quad (1)$$

where L is the FSO link length and R_{arm} is the height of the collimator mount. With this in mind, if we consider an FSO link of 5 km and $R_{arm} = 44.4$ mm (Thorlabs' KM100), a precision of 0.1 mm in the receiver, requires a motor precision of roughly 1 nm, which is within the precision range of commercial stepper-motor actuators [55].

After implementing the ATP system, several algorithms can be considered for the automatic alignment of the link. To

²For simplicity, in this work and in our referenced work of [44], no ATP mechanism has been considered for the receiver collimator. However, in a practical scenario, the most robust implementation should rely on the usage of a unified control loop simultaneously actuating over the vertical and horizontal axes of the transmitter and receiver collimators and/or lenses.

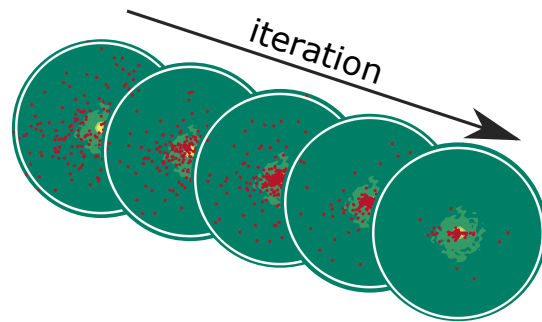


Fig. 6. Qualitative depiction of the evolution of the PSO algorithm when applied for automatic optical beam alignment. The red dots indicate the position of the particles generated by PSO on each iteration, which are plotted over contour maps of pre-calibrated received optical power.

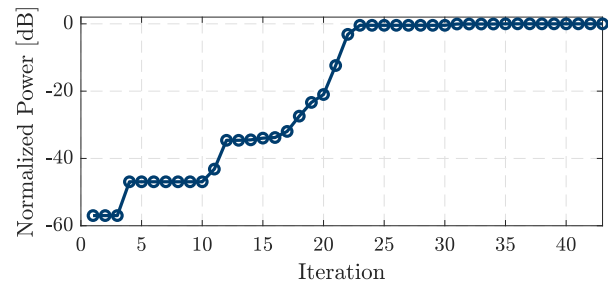


Fig. 7. Evolution of normalized received optical power as a function of the number of PSO iterations.

that end, classical control theory can be successfully utilized, provided that the system is characterized by a well-defined dependence between received optical power and incremental motion of the actuators. However, as previously exposed in Fig. 2, the extreme sensitivity of the optical beam alignment process imposes that quasi-null received optical powers are obtained for minor alignment errors in the range of 1–2 mm. Therefore, it might likely happen that the initial starting position for the optical alignment process corresponds to a wide region of null or quasi-null received optical power, where the derivative of the optimization function is ill-defined, thereby hindering the convergence of most classical control algorithms, which might get easily stuck within meaningless local minima. In order to circumvent this limitation, state-of-the-art AI algorithms can be considered as a robust alternative solution for this challenging problem, enabling to treat the optical alignment optimization using a black-box methodology that enables the receiver discovery with no previous system knowledge. In that sense, in [44], we proposed and experimentally demonstrated the successful alignment of a gimbal-based FSO system using a particle swarm optimization (PSO) algorithm starting from a position of null received optical power.

Fig.6 qualitatively exposes the functionality of the PSO algorithm when applied to this scenario. In the first iterations of the alignment process, the PSO particles are spread throughout the whole search space, ensuring that a position of significant received optical power is found. Then, as the algorithm converges, the particles become concentrated in the optimum alignment point, *i.e.* the point returning the

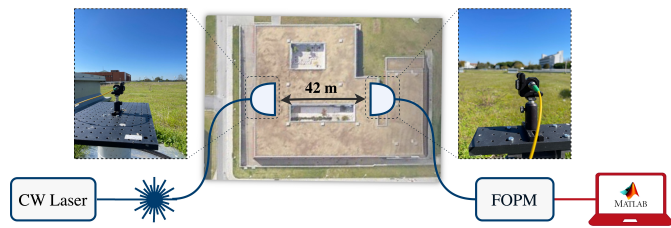


Fig. 8. Experimental setup for outdoor FSO transmission over 42 m.

highest received optical power. The respective progression of normalized power with increasing number of iterations is depicted in Fig.7. As expected, the received power monotonically increases with the number of iterations, achieving optimum convergence after approximately 23 iterations.

III. FSO TRANSMISSION UNDER ATMOSPHERIC TURBULENCE: CHANNEL MODELLING AND ESTIMATION

Having discussed the main requirements and solutions for FSO beam alignment in the previous section, let us now address the impact of atmospheric turbulence, which represents one of the major challenges associated with the design of FSO systems. First, we will elaborate on the modelling of atmospheric turbulence, resorting to experimental data collected from a permanent outdoor FSO link. Then, taking advantage of the insights gained from the modelling effort, we will devise optimized channel estimators that enable to accurately track and predict the evolution of received optical power under turbulent conditions.

A. Experimental Modelling of Outdoor FSO Systems

With the aim of experimentally modelling an FSO system under varying meteorological conditions, the experimental setup exhibited in Fig. 8 was assembled. This setup consists of a continuous wave laser source operating at 1550 nm with 13 dBm output power, followed by a seamless air-to-fiber link, implemented with a pair of passive fiber collimators, similar to the ones utilized in the previous section (F810-1550APC). The collimators are set on a high-inertia mounting base for improved stability while being distanced by 42 m of uninterrupted free-space on the rooftop of our research center. The received optical power is then measured by an in-house developed fast optical power meter (FOPM), capable of measuring and digitizing received optical power at sampling rates of up to 160 kHz.

To start the experimental modelling of the FSO system, we have set a week-long measurement procedure at a sampling rate of 1 Hz, to obtain a broader vision of the link stability over time. The results of the week-long measurements are exposed in Fig. 9. The scintillation effect on the link can be clearly observed, as the daytime measurements demonstrate a greater level of power fluctuations when compared to nighttime, thus indicating a greater level of turbulence, which is in accordance with other recent experimental observations [52] and with the fundamental knowledge on the diurnal dynamics of turbulent kinetic energy [56]. Nevertheless, despite the

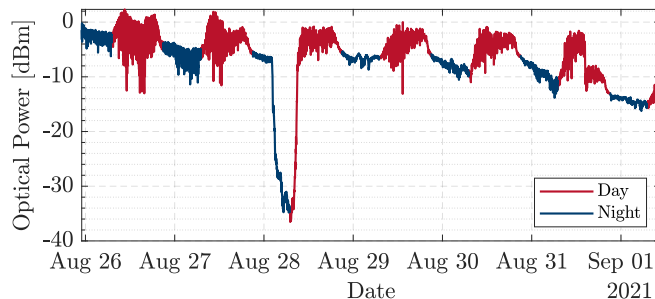


Fig. 9. Week-long optical power measurements obtained from the FSO link depicted in Fig. 8.

lower scintillation during nighttime, we can also observe that the average received optical power tends to be reduced by approximately 3–4 dB when compared to daytime. Although counterintuitive, this phenomenon can be attributed to the significant changes in temperature and humidity from day to night, which might have a strong impact on the coupling losses at the optical collimators. The obtained data also shows a significant power drop on the 28th August, likely due to reduced visibility and/or humidity on the collimator lens. It is also possible to assess that the alignment tends to deteriorate over time, as the initial measurements indicate a received optical power level slightly above 0 dBm, whereas in the final measurements the system is already receiving optical power levels under -12 dBm.

As a whole, the big picture provided by the long-term measurements in Fig. 9 clearly exposes the interplay between different phenomena that co-occur at rather different time scales. The faster optical power variations are most likely to be associated with the impact of atmospheric turbulence, with expected correlation times in the ms range. On top of this fast scintillation effect, a repetitive slow fading behaviour can also be identified, corresponding to a rather long coherence period that can exceed several hours. This slow fading phenomenon can be associated with the varying meteorological conditions, daily changes of temperature, pressure and humidity, as well as a slow misalignment effect over time. In order to better model and mitigate these optical power fluctuations in realistic outdoor FSO links, it is therefore of utmost importance to somehow distinguish between the different sources of received optical power variation.

Having observed the combined effect of different sources of FSO power loss on a long timescale, let us now focus our analysis on an hour-long dataset representative of a day-to-night transition period, taken at 21–22 PM of 14th September 2021. In order to obtain further insight into the impact of atmospheric turbulence, the FOPM has now been set with a sampling rate of 10 kHz, thereby allowing to capture the coherence time of turbulence-induced scintillation.

In order to facilitate the comparison of the experimentally measured data against well-known numerical models of atmospheric turbulence, we will resort to the definition of normalized irradiance, I , which can be obtained from the

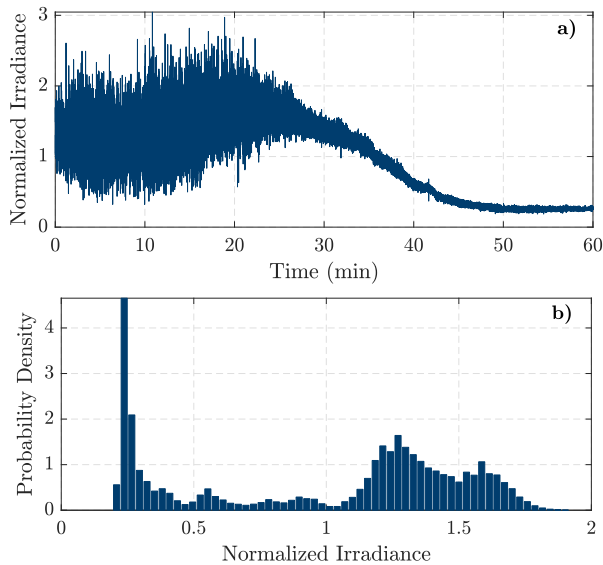


Fig. 10. Experimentally measured normalized irradiance values obtained from the 42 m outdoor FSO link depicted in Fig. 8 during 1-hour (14 September 2021, 22PM) at a sampling-rate of 10 KHz. a) measured normalized irradiance over 60 min; b) probability density of measured normalized irradiance.

received optical power, P , simply as

$$I(t) = P(t)/\overline{P(t)}, \quad (2)$$

where $P(t)$ is the received optical power in Watts over time, t , and $\overline{P(t)}$ is the average received optical power within a given measurement window.

Figure 10a depicts the normalized received irradiance in a 60-minute period, demonstrating the system fading from a stronger turbulent condition into weaker turbulence at nighttime. As previously observed in the week-long measurements, a clear slow-fading effect can be identified on the normalized irradiance of Fig. 10a. In order to better understand how the variations of normalized irradiance are distributed, in Fig. 10b we present a histogram of the measured data, where it can be clearly observed that the normalized irradiance is composed of the superposition of several probability density distributions. As a consequence, it is impossible to directly fit these data against theoretical turbulence models, which are aimed at describing the impact of scintillation under well-defined atmospheric turbulence regimes.

To correct this issue and enable a more precise modelling of the fading system, we followed a strategy involving the dissociation between fast and slow fading effects from the dataset. The slow-fading effects can be isolated by applying a moving average filter with 100 ms time window (large enough to avoid erasing any turbulence-induced fading) over the measured normalized irradiance. The result of this process is illustrated in Fig. 11, where the two estimated components of the received normalized irradiance, i.e. slow-fading and turbulence-induced fading, are isolated. Therein, it can be seen that the estimated turbulence-induced fading now shows a stabilized distribution of normalized irradiance that is always centered around unity. It is worth emphasizing

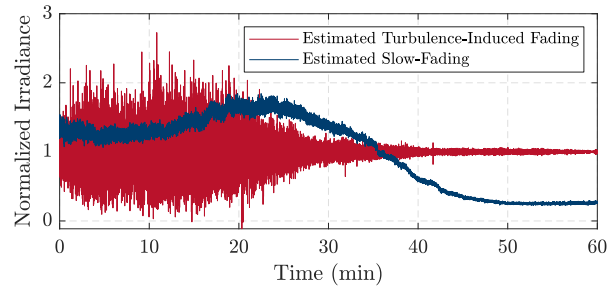


Fig. 11. Estimated contribution of the slow-fading (>100 ms coherence time) and turbulence-induced fading contributions to the measured irradiance data shown in Fig. 10

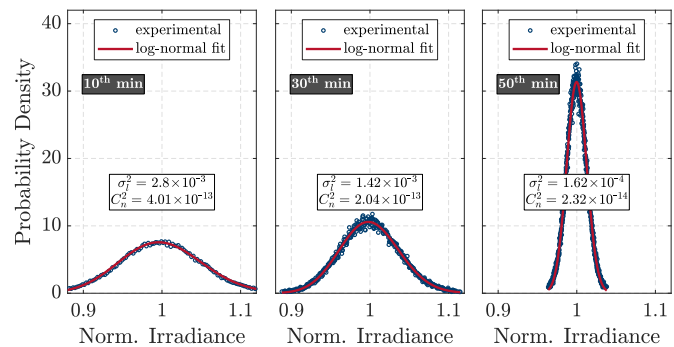


Fig. 12. Experimental and theoretical (log-normal) probability density functions of the scintillation effect caused by atmospheric turbulence. Measurements are split in 1-minute periods, and three examples are shown: i) 10th min; ii) 30th min; iii) 50th min.

that the proposed methodology for the separation between slow and fast variations of received optical power does not guarantee that the whole contribution of the *fast scintillation* effects can be fully attributed to atmospheric turbulence. Indeed, other μ s/ms-scale effects (e.g. mechanical vibrations inducing random pointing errors) might still be captured under the *fast* component. The relative impact of these other unknown sources of optical power fluctuation will be progressively reduced as the FSO link distance increases, rendering turbulence as the dominant effect.

Using the estimated turbulence-induced fading, we can now perform the quantitative assessment of atmospheric turbulence levels throughout the dataset, resorting to experimental fittings against the log-normal model [36]. The fit between the fast-fading experimental data and the log-normal model was then evaluated for 1-min intervals, with a few 20-min evenly-spaced examples being represented in Fig. 12. The estimated Rytov variances, σ_l^2 , for each data set are also indicated, as well as the respective refractive-index structure parameter, C_n^2 , calculated as,

$$C_n^2 = \frac{\sigma_l^2}{1.23 \left(\frac{2\pi}{\lambda}\right)^{7/6} L^{11/6}}, \quad (3)$$

where $\lambda = 1550$ nm is the signal wavelength and $L = 42$ m is the transmission distance.

Finally, in Fig. 13 we present the evolution of the estimated σ_l^2 and C_n^2 parameters throughout the dataset, confirming the qualitative observation that the turbulence level has indeed

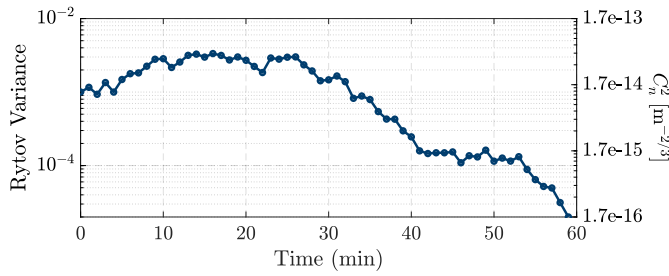


Fig. 13. Estimated Rytov variance and refractive index structural parameter C_n^2 from fitting of the experimental data against a log-normal theoretical reference, calculated in 1-min intervals.

decreased during the selected turbulence transition period. From the observation of Fig. 13, it can be concluded that $10^{-5} < \sigma_l^2 < 10^{-2}$, which corresponds to a low turbulence regime, as expected for a short link length of 42 m. In addition, the range of atmospheric refractive-index structure parameter, $10^{-16} < C_n^2 < 10^{-13}$, is well matched with the typical values found in other FSO turbulence studies [31], spanning from low ($C_n^2 \simeq 10^{-16} \text{ m}^{-2/3}$) to average ($C_n^2 \simeq 10^{-14} \text{ m}^{-2/3}$) turbulence, which further confirms that while the turbulence phenomena is indeed present on the link, its manifestation in terms of received optical power variance is minor due to the low link length (note the $L^{11/6}$ dependence of the Rytov variance in (3)). Also note that, for the range of measured Rytov variances, the scintillation index,

$$\sigma_N^2 = \exp\left(\frac{0.49\sigma_l^2}{\left(1 + 1.11\sigma_l^{12/5}\right)^{7/6}} + \frac{0.51\sigma_l^2}{\left(1 + 0.69\sigma_l^{12/5}\right)^{5/6}}\right) - 1, \quad (4)$$

is almost equals to the Rytov variance, $\sigma_N^2 \simeq \sigma_l^2$ [57].

B. Designing Accurate Channel Estimation Tools

Having thoroughly analyzed the characteristics of the outdoor FSO link under test, namely, the atmospheric turbulence and the slow-fading effects, we can now proceed by exploiting the time-correlation inside the FSO channel to design estimation tools that can accurately predict the evolving state of the channel. To this intent, let us start by considering a static model composed of a moving average filter, similarly to the strategy employed in our previous work [15], where the estimation of the normalized irradiance, I_p , is performed as,

$$I_p(n+1) = \frac{1}{M+1} \sum_{k=0}^M I(n-k), \quad (5)$$

such that the predicted irradiance at time instant $n+1$ is estimated at the expense of M previous irradiance measurements, where M represents the memory of the predictor. Although it provides a low complexity channel estimation, this moving average estimator suffers from two main drawbacks:

- i) it inherently considers a fixed M time window, thus requiring *a priori* characterization of the channel memory. For the same reason, even if well calibrated to the initial

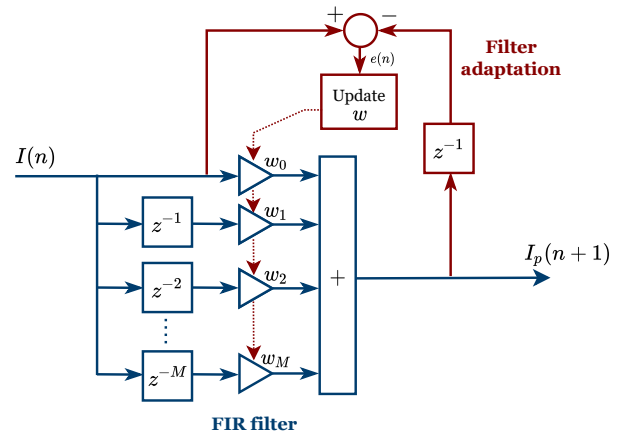


Fig. 14. Schematic representation of the proposed adaptive channel estimator for the FSO channel. The forward channel estimation is represented in blue, whereas the red blocks represent the feedback loop that implements the updating of the filter weights.

conditions of the channel, the moving average estimator is not able to self-adapt to time-dependent changes of channel memory, which, as we have seen in the previous section, might be a prominent characteristic of realistic outdoor FSO channels;

- ii) by using a rectangular window, the moving average estimator inherently considers the same weight for every M past irradiance measurements, which would correspond to an unrealistic brick-wall auto-correlation function for the channel.

In order to circumvent the aforementioned limitations, we now consider an alternative methodology for channel estimation, resorting to the use of an adaptive filter, which performs an automatic adjustment of the filter weights, w_k , to the sensed channel under test, following the minimization of a cost function that captures the error between the estimated and previously measured irradiance values,

$$I_p(n+1) = \sum_{k=0}^M w_k(n) \cdot I(n-k). \quad (6)$$

In order to produce an adaptive model, the filter weights, w_k , must be continuously updated to minimize the estimation error. From the plethora of methods for error minimization, let us consider two common approaches: the least mean-squares (LMS) and recursive least-squares (RLS) cost functions. In the LMS methodology, the weight update is given by,

$$w_k(n+1) = w_k(n) + 2\mu I(n-k)e(n), \quad (7)$$

where μ is the step-size and $e(n) = I(n+1) - I_p(n+1)$ is the measured prediction error. Alternatively to the LMS approach, the RLS cost function provides a solution for the weight update of an adaptive filter, with the advantage of enabling a faster convergence,

$$w_k(n+1) = w_k(n) + K_k(n)e(n), \quad (8)$$

where K is a gain factor that depends on the input signal and its auto-correlation.

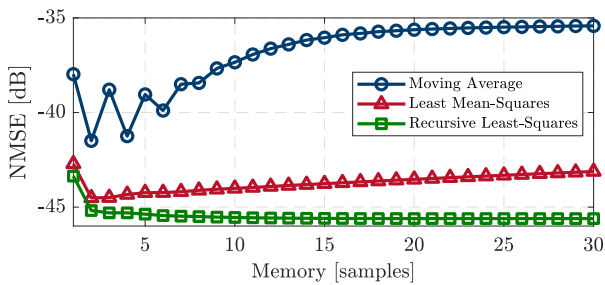


Fig. 15. Accuracy (NMSE between predicted and actually measured values) of the proposed FSO channel estimators as a function of the memory length included in the filter.

Note that, the channel estimation task can be conveniently performed at a modest update rate in the KHz range, whereas most low-end microcontrollers easily support serial processing speeds of several MHz. It is therefore assumed that the update of the filter taps at time instant $n + 1$, $w_k(n + 1)$, following expressions (7) or (8), can be performed *immediately after* the measurement of the irradiance value at this same time instant, $I(n + 1)$, which will then be utilized to predict the irradiance value in the next time instant, $I_p(n + 2)$. A block diagram depicting the practical implementation of the adaptive channel estimator is shown in Fig. 14.

To verify the performance of the proposed channel estimators, let us consider their application over the experimental dataset presented in Fig. 10. The channel estimation performance is quantified through the normalized mean square error (NMSE) between the estimated and measured irradiances,

$$\text{NMSE [dB]} = 10 \log_{10} \left(\frac{\sum (I_p - I)^2}{\sum I_p^2} \right), \quad (9)$$

As a rule of thumb, it is typical to consider that an NMSE below -40 dB represents a very accurate model.

Figure 15 depicts the obtained NMSE performance with the three proposed channel estimators (moving average and LMS/RLS adaptive equalizers) as a function of the memory length, M , introduced in the model. As expected, the simpler non-adaptive moving average filter leads to the worse estimation performance, also evidencing a strong dependence on the channel memory, owing to the fact that all filter coefficients are equally weighted. As a consequence, if the defined memory length, M , is too large, then the estimator becomes too slow, preventing to capture the shorter coherence times associated with the atmospheric turbulence. On the opposite hand, if the memory length is too short, then the channel estimator loses its ability to adequately ponder the relative impact of the simultaneous occurrence of slow and fast optical power variations. In contrast, the adaptive channel estimators provide the best channel estimation performance and an improved independence on the selected value of M , since the filter weights are automatically adapted over time, thereby enabling to operate with a large enough memory length without incurring into performance penalty. As expected, the RLS variant shows a slightly improved performance, mainly owing to its improved convergence, even

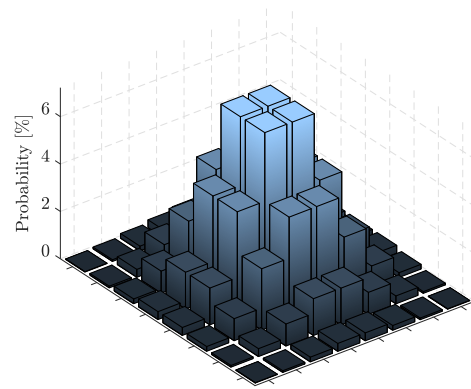


Fig. 16. Probability distribution of the transmitted PCS-64QAM with an entropy of 5 bits per symbol.

though the additional implementation complexity might not justify its choice against the simpler LMS equalizer.

IV. 800G+ COHERENT FSO OUTDOOR TRANSMISSION

After addressing the isolated impact of pointing errors and atmospheric turbulence in sections II and III, in this section, we provide a long-term (48 hours) experimental demonstration of a coherent FSO system transmitting at more than 800 Gbps in an outdoor deployment. By assessing the achievable information rate (AIR) over the outdoor FSO link under varying weather conditions, we aim at demonstrating the potentiality of leveraging ultra-high capacity FSO communications on the next generation of 800G fiber-optics transceivers, which is already under development [58], [59].

A. Transmitted Signal: Probabilistic Constellation Shaping

In order to tighten the gap to Shannon capacity, in this experimental demonstration, we will consider the use of probabilistic constellation shaping (PCS) [60], a state-of-the-art modulation technique that is already being integrated into the latest generation of coherent optical transceivers [58]. In short, PCS allows to approximate the maximum capacity of additive white Gaussian noise (AWGN) channels by attributing amplitude-dependent probabilities to each symbol of a standard QAM constellation, thereby transforming the transmitted signal into a Gaussian-like distribution of symbols, which, according to Shannon's seminal theory, allows approaching the maximum capacity of AWGN channels. Instead of the identically distributed symbols of uniform QAM signal, whose symbol probability is equal for all constellation points, in PCS constellations, the probability of occurrence of each transmitted symbol, x_n , is given by the Maxwell-Boltzman distribution [61],

$$P_{x_n} = \frac{\exp(-\lambda|x_n|^2)}{\sum_{n=1}^M \exp(-\lambda|x_n|^2)}, \quad (10)$$

where M is the constellation size and $\lambda \geq 0$ is the so-called *shaping parameter* that controls the shape of the probability distribution as a function of the amplitude of the transmitted symbols, $|x_n|^2$.

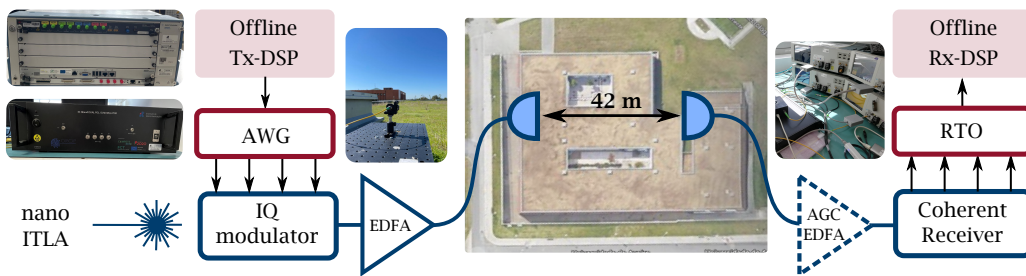


Fig. 17. Experimental setup utilized to demonstrate a coherent FSO link in an outdoor deployment capable of achieving 800G+ data-rate. The central inset depicts a top view of Instituto de Telecomunicações building, taken directly from Google Maps (<https://tinyurl.com/vff4syse>).

As a consequence of the Gaussian constraint imposed upon the transmitted signals, the maximum entropy that can be transmitted over the PCS constellation is given by,

$$E = - \sum_{n=1}^M P_{x_n} \log_2(P_{x_n}). \quad (11)$$

It is worth noting that for the case of uniform modulation, where $P_{x_n} = 1/M$, expression (11) leads to the well-known $\log_2(M)$ number of bits per symbol supported by uniform M -QAM constellations.

In this work, we will employ a PCS-64QAM constellation whose shaping parameter is defined so that the entropy of the transmitted signal, E , is set to an average of 5 bits per symbol. The respective probability distribution of the generated PCS constellation is shown in Fig. 16, which has been obtained resorting to the well-known constant composition distribution matcher (CCDM) [62]. The 5-bit PCS-64QAM constellation is then transmitted at a baud-rate of 92 Gbaud over the two orthogonal polarization modes, thus enabling for a maximum AIR of 920 Gbps in an ideal noiseless channel.

B. Experimental Setup and Digital Signal Processing

The experimental setup used to demonstrate 800G+ outdoor FSO transmission is depicted in Fig. 17. The 92 Gbaud PCS-64QAM signal is first subjected to root-raised cosine (RRC) pulse shaping with 0.1 roll-off and then upsampled to 120 Giga-samples-per-second (Gsp/s) (~ 1.3 samples per symbol). The signal is then uploaded to an arbitrary waveform generator (AWG) with ~ 45 GHz analog bandwidth and 120 Gsp/s sample rate (Keysight M8194A). A dual-polarization IQ modulator with 35 GHz bandwidth implements the modulation of the digital signal into an optical carrier generated by a nano-integrated tunable laser assembly (nano-ITLA, output power 13 dBm, wavelength 1545 nm). The resulting optical signal is then amplified by an Erbium-doped fiber amplifier (EDFA), before being sent to free-space by a fiber collimator (Thorlabs F810APC-1550). After 42 m of free-space propagation over the same outdoor FSO link utilized in section III (see Fig. 8), the free-space signal is then directly collimated into the fiber core. Afterwards, the signal is O/E converted by a coherent optical receiver with 70 GHz bandwidth, with the resulting electrical signal being sampled and digitized by a 4-channel real-time oscilloscope (RTO), with 200 Gsp/s sample rate and 70 GHz bandwidth (Tektronix DPO77004SX).

After digitization in the RTO, the received signal is directly transferred to a workstation and offline processed in MATLAB, including the standard digital signal processing (DSP) subsystems that are commonly employed in coherent optical transceivers, namely:

- i) digital deskew of the I/Q components on both polarization to account for the timing skew introduced by the slightly different RF cable lengths (from the output of the balanced photodiodes in the coherent receiver and the input of the RTO analog channels);
- ii) correction of I/Q amplitude imbalance through Gram-Schmidt orthonormalization [63];
- iii) removal of the direct-current (DC) component introduced by the coherent receiver;
- iv) resampling of the 120 Gsp/s received signal to 2 samples per symbol, *i.e.* 184 Gsp/s;
- v) low-pass filtering to eliminate out-of-band noise, using a 10th-order Gaussian filter with 55 GHz cut-off frequency;
- vi) polarization demultiplexing, bandwidth equalization, timing recovery and residual I/Q skew (from the receiver) compensation using a 4×4 real-valued 15-taps adaptive equalizer [64] driven by a radius-directed cost function [65];
- vii) frequency-offset estimation and compensation using a frequency-domain technique to determine the spectral peak of the demodulated signal [66];
- viii) removal of the DC component of the transmitter using a moving average filter;
- ix) carrier-phase estimation and removal using a pilot-based approach [67] with an averaging window of 101 symbols;
- x) fine-tuning of the adaptive equalization performed in step vi) resorting to a 4×4 real-valued least mean squares (LMS) adaptive equalizer [68] with 51 taps;
- xi) downsampling to 1 sample per symbol;
- xii) symbol demapping and numerical evaluation of the generalized mutual information (GMI) [69] between the transmitted and received (after the DSP chain) signals, which provides an achievable information rate (AIR) for coherent optical systems employing ideal soft-decision bitwise decoding [70].

In order to decouple the potential DSP performance fluctuations from the desired analysis of the FSO channel performance, we have considered a *genie-aided* DSP implementation, *i.e.* the DSP convergence is guaranteed by a fully data-aided approach.

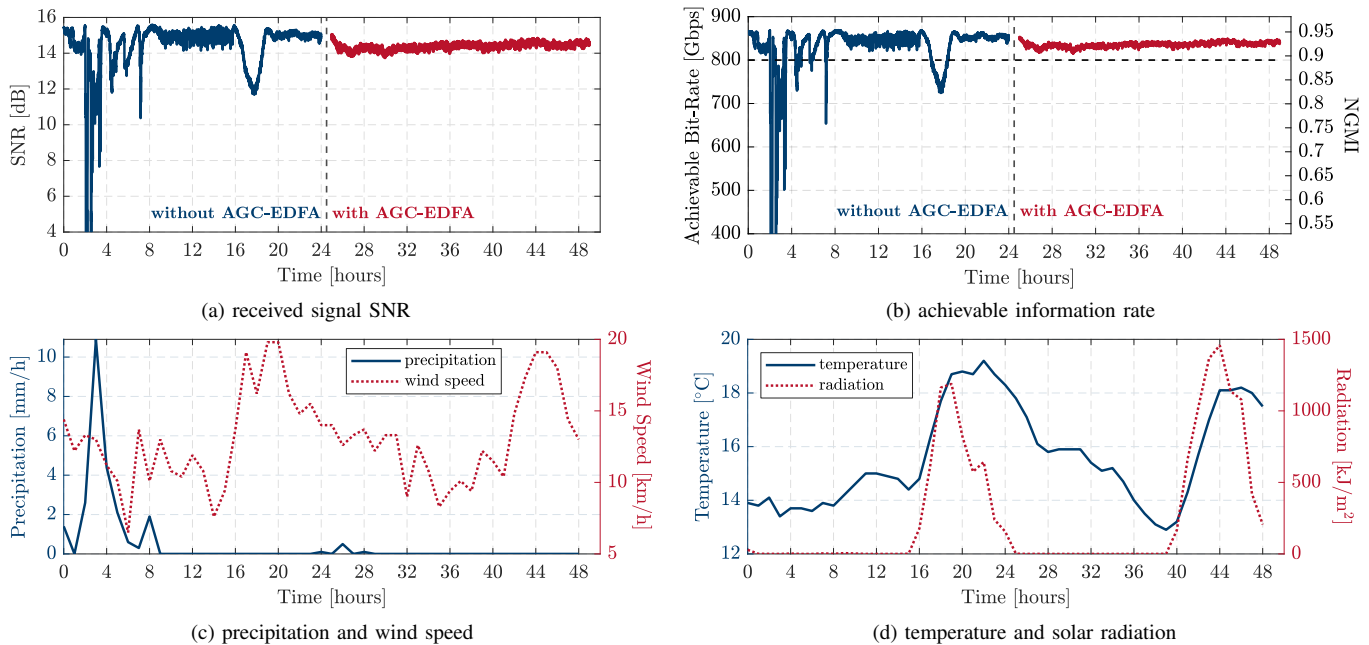


Fig. 18. Experimental measurements obtained during a 48-hour outdoor FSO transmission of a 5-bit PCS-64QAM at 92 Gbaud with and without an AGC-EDFA at the receiver side. a) signal-to-noise ratio of the received signal; b) achievable bit rate and NGMI, related through expression (12); c) measured precipitation rate and wind speed; d) measured temperature and solar radiation.

The transmission over the FSO channel is then performed continuously over a period of approximately 48-hours, since the AWG enables the continuous playback of the uploaded transmitted signal, with a memory of 512 Ksamples. At the receiver side, the RTO is repeatedly triggered to acquire batches of 500 Ksamples of the received signal in periods of approximately 20 s, which corresponds to the minimum period required to perform the communication with the RTO and to apply the set of DSP subsystems described above. This leads to a critical issue associated with the accessible time scales for the offline performance analysis of FSO systems supported by high-baudrate coherent receivers: while on the one hand, the time window of each data acquisition is very short ($2.5 \mu\text{s}$ in this work); on the other hand, the feasible time interval between data acquisitions is in the order of several seconds, due inevitable delays imposed by the interfacing with the RTO and the offline DSP processing. Due to these rather distant time scales, it becomes quite challenging to properly study the impact of atmospheric turbulence (which, as stated before, is characterized by a typical coherence time in the ms range) using offline coherent reception. In particular, the impact of turbulence-induced phase fluctuations on the received signal would be of major interest, given the phase-sensitiveness of coherent receivers. To that end, real time operation is definitely the most adequate choice, in order to avoid the long time intervals between captured data. However, due to the lack of commercial-off-the-shelf (COTS) transceivers operating at ultra-high data rates of 800 Gbps, in this work, we will limit our analysis to the aforementioned offline processing paradigm. Therefore, and considering the low turbulence regime revealed by the experimental modelling of the outdoor FSO link presented in section III, the main aim of

this 800G experimental assessment is to analyze and partially compensate the impact of the slow-fading phenomena, which, in section III, has already been identified as an important performance issue.

Targeting the mitigation of the slow-fading associated with the long-term measurements of received optical power in the outdoor FSO link, we will consider two variants for the receiver architecture:

- i) an unamplified coherent receiver, whose received optical power is directly dictated by the time-varying losses of the FSO link;
- ii) a pre-amplified coherent receiver, using an EDFA with automatic gain control (AGC), which tries to automatically adapt its gain (through the operating current) so that the received optical power remains at a fixed value of 3 dBm. The AGC-EDFA allows a maximum gain of approximately 20 dB with 4 dB noise figure.

C. Experimental Results

Following the continuous 48-hour measurement of system performance using the coherent FSO setup described above, the obtained experimental results are summarized in Fig. 18. Therein, in the upper row, we show the estimated SNR of the received signal (directly obtained from the error vector magnitude of the received signal after processing) in Fig. 18a and the respective normalized GMI (NGMI) and achievable bit rate in Fig. 18b. Note that the achievable bit rate, R_b , is directly related to the measured NGMI as,

$$R_b = 2R_s \left(E - \log_2(M) (1 - \text{NGMI}) \right), \quad (12)$$

where $R_s = 92$ Gbaud is the baudrate, $E = 5$ is the transmitted entropy and $M = 64$ is the constellation size. The measurements occurred during the winter of 2021, from 4:53PM of 20th December and 5:52PM of 22th December. The time axis in Fig. 18 is then defined relatively to the starting date of the measurements. A gap of approximately 1-hour has been carried out when switching from the unamplified receiver configuration to the pre-amplified receiver, using the AGC-EDFA. The meteorological conditions registered by a meteorological mast located nearby the deployed FSO link (less than 100 m) are shown on the bottom row of Fig. 18, including the precipitation rate, wind speed (see Fig. 18c), temperature and solar radiation (see Fig. 18d). The hourly meteorological readouts are official measurements made available by the Portuguese Institute for Sea and Atmosphere (IPMA) through its online platform [71].

Let us start by analyzing the system performance with the unamplified coherent receiver, *i.e.* without the AGC-EDFA, corresponding to the first 24-hour period. From the achievable bit rate measurements, we can observe that under the best channel conditions, bit rates above 850 Gbps are achievable. However, when the channel conditions are degraded, two sets of significant drops of performance can be identified: the first, coinciding with precipitation peaks registered between the 2nd and 9th hours of measurement; the second, coexisting with the temperature rise and solar radiation peak registered between the 17th and 20th hours. The measured SNR values for these periods show recurrent losses of 3–5 dB, which lead to a decrease of the achievable bit rate by approximately 100–150 Gbps. In the worst-case scenario, corresponding to the heavy rain condition experienced between the 3rd and the 4th hour, the SNR drops below operational levels, leading to very high losses of bit rate³. Note that, for ease of visualization, bit rate values below 400 Gbps are deemed as loss of signal, and therefore are not shown in Fig. 18b. These measurements clearly expose the impact of the slow-fading phenomena associated with varying meteorological conditions on the performance of an outdoor FSO link, which severely limits the communication reliability at high bit rates.

In order to try to mitigate the impact of this slow-fading phenomenon, and following the seminal works of [9], [72], in the second half of the measurement period we have introduced a pre-amplifier EDFA, whose pump current is controlled by a fast (analog) AGC circuit, thereby attempting to maintain the received optical power at a fixed value of 3 dBm (near-optimal for the coherent optical receiver). As a consequence, we can observe that the performance of the FSO link has remained significantly more stable during the whole measurement period, allowing to keep an achievable bit rate above the targeted 800 Gbps at all times. Although minor precipitation rates have been registered during this former period of 24-hour measurements, the increased long-term stability of the received

SNR and NGMI is apparent, namely during the periods of larger temperature change and solar radiation. As previously demonstrated in [9], [72], it can therefore be concluded that the use of a pre-amplifier EDFA can indeed contribute to an improved robustness of the outdoor FSO link to the impact of slow-fading interferences, thereby enabling to keep 800G-capable communications with 100% reliability during the latter 24-hour measurement period. Nevertheless, the extent up to which the atmospheric turbulence can actually be mitigated by this approach is not yet totally clear, with some recent works suggesting the replacement of the pre-amplifier EDFA by a semiconductor optical amplifier (SOA) [73], [74], whose faster gain response might provide further stabilization of the link under stronger turbulence conditions.

V. CONCLUSION

We have reviewed the key challenges and opportunities associated with the development of ultra-high capacity FSO systems, focusing on the open research topics of high-precision adaptive optical beam steering and on the modelling and mitigation of atmospheric turbulence and other meteorological phenomena. A particular opportunity for high-capacity FSO systems arises through the adoption of a seamless convergence with the fiber-based infrastructure, thereby benefiting from the reutilization of mature and highly competitive technology. In this regard, an outstanding opportunity lies in the possibility of exploiting the convergence of FSO systems with the latest generation of digital coherent optical transceivers, leveraging on a decade of remarkable progress, both in terms of bandwidth provisioning – soon enabling per-channel bit-rates of 800 Gbps and above – and cost reduction – now entering the competitive short-reach market. This promising alliance shows the potential to provide an unprecedented capacity to next-generation FSO systems, which might become a decisive factor for its successful deployment in novel bandwidth-hungry applications, namely within the framework of 6G and/or satellite-based communications.

Nevertheless, there are still several critical challenges to be overcome, among which the major concern goes to the reduced reliability of FSO links. Despite the blooming of encouraging results that are being constantly reported, novel solutions must still be developed and refined. In this work, we have focused our attention on a particularly critical issue that is fundamental for solving the reliability limitations of FSO systems: the modelling and mitigation of the distortions associated with the free-space channel. Through the long-term experimental analysis of a 42 m outdoor FSO link, we have exploited the interplay between atmospheric turbulence and other slow-fading phenomena, devising optimized channel estimators for a highly accurate prediction of the varying conditions of the FSO channel over time, which can be used in favor of designing more robust signal transmission (e.g. adaptive modulation and/or coding) and active mitigation techniques (e.g. pre- and/or post-amplification of the signal). Culminating the work developed in this paper, we have experimentally demonstrated the transmission of an 800G+ signal over the FSO link under test, achieving ultra-high reliability against

³It is important to refer that the SNR degradation suffered during the rainy periods is mostly attributed to the fully exposed collimator lenses, which tend to accumulate water droplets on their surface, thereby refracting the transmitted and/or received beams, and thus severely attenuating the received optical power. A significant mitigation of this effect is expected if the collimator lenses are somehow protected from direct contact with rain.

slow-fading effects through the use of a pre-amplified coherent receiver with automatic gain control.

As a whole, the results presented in this work demonstrate that the exploitation of the distinctive features of digital coherent transceivers might provide the required traction to leverage the development of the next generation of FSO systems. A set of novel upcoming opportunities for the exploitation of this technology are very likely to flourish during the current and next decade, including terrestrial (6G) and space communications (both satellite-to-satellite and satellite-to-earth), where the unprecedented spectral efficiency enabled by coherent detection might prove instrumental to cope with the requirements of multiple Terabit-per-second wireless data-rates. Through a seamless convergence with the wired fiber-based telecom infrastructure, coherent optical wireless systems will benefit from a major opportunity: the inheritance of advanced but matured communication technologies and components, which can decisively accelerate its short-term deployment.

REFERENCES

- [1] M. Agiwal, A. Roy, and N. Saxena, "Next generation 5G wireless networks: A comprehensive survey," *IEEE Commun. Surveys Tuts.*, vol. 18, no. 3, pp. 1617–1655, 2016.
- [2] S. Chen, Y.-C. Liang, S. Sun, S. Kang, W. Cheng, and M. Peng, "Vision, requirements, and technology trend of 6G: How to tackle the challenges of system coverage, capacity, user data-rate and movement speed," *IEEE Wireless Commun.*, vol. 27, no. 2, pp. 218–228, apr 2020.
- [3] M. Z. Chowdhury, M. Shahjalal, S. Ahmed, and Y. M. Jang, "6G wireless communication systems: Applications, requirements, technologies, challenges, and research directions," *IEEE Open J. Commun. Soc.*, vol. 1, pp. 957–975, 2020.
- [4] M. Z. Chowdhury, M. T. Hossain, A. Islam, and Y. M. Jang, "A comparative survey of optical wireless technologies: Architectures and applications," *IEEE Access*, vol. 6, pp. 9819–9840, 2018.
- [5] A. S. Hamza, J. S. Deogun, and D. R. Alexander, "Classification framework for free space optical communication links and systems," *IEEE Commun. Surveys Tuts.*, vol. 21, no. 2, pp. 1346–1382, 2019.
- [6] R. Zhang, X. Tang, C.-W. Hsu, Y.-W. Chen, and G.-K. Chang, "Semi-supervised and supervised nonlinear equalizers in fiber-FSO converged system," *J. Lightw. Technol.*, vol. 39, no. 19, pp. 6175–6181, oct 2021.
- [7] M.-C. Jeong, J.-S. Lee, S.-Y. Kim, S.-W. Namgung, J.-H. Lee, M.-Y. Cho, S.-W. Huh, Y.-S. Ahn, J.-W. Cho, and J.-S. Lee, "8 × 10-Gb/s terrestrial optical free-space transmission over 3.4 km using an optical repeater," *IEEE Photon. Technol. Lett.*, vol. 15, no. 1, pp. 171–173, jan 2003.
- [8] P.-L. Chen, S.-T. Chang, S.-T. Ji, S.-C. Lin, H.-H. Lin, H.-L. Tsay, P.-H. Huang, W.-C. Chiang, W.-C. Lin, S.-L. Lee, H.-W. Tsao, J.-P. Wu, and J. Wu, "Demonstration of 16 channels 10 Gb/s WDM free space transmission over 2.16 km," in *Digest of the IEEE/LEOS Summer Topical Meetings*, 2008.
- [9] E. Ciaramella, Y. Arimoto, G. Contestabile, M. Presi, A. D'Errico, V. Guarino, and M. Matsumoto, "1.28 Terabit/s (32×40 Gbit/s) WDM transmission system for free space optical communications," *IEEE J. Sel. Areas Commun.*, vol. 27, no. 9, pp. 1639–1645, Dec. 2009.
- [10] G. Parca, A. Shahpari, V. Carozzo, G. M. T. Belleffi, and A. L. J. Teixeira, "Optical wireless transmission at 1.6-Tbit/s (16×100Gbit/s) for next-generation convergent urban infrastructures," *Optical Engineering*, vol. 52, no. 11, p. 116102, 2013.
- [11] X. Feng, Z. Wu, T. Wang, H. Jiang, Y. Su, H. Jiang, and S. Gao, "120 Gbit/s high-speed WDM-QPSK free-space optical transmission through 1 km atmospheric channel," *Electronics Letters*, vol. 54, no. 18, pp. 1082–1084, 2018.
- [12] A. Dochhan, J. Poliak, J. Surof, M. Richerzhagen, H. F. Kelemu, and R. M. Calvo, "13.16 Tbit/s free-space optical transmission over 10.45 km for geostationary satellite feeder-links," in *Photonic Networks; 20th ITG-Symposium*, 2019.
- [13] H.-W. Wu, H.-H. Lu, W.-S. Tsai, Y.-C. Huang, J.-Y. Xie, Q.-P. Huang, and S.-C. Tu, "A 448-Gb/s PAM4 FSO communication with polarization-multiplexing injection-locked VCSELs through 600 m free-space link," *IEEE Access*, vol. 8, pp. 28 859–28 866, 2020.
- [14] A. Lorences-Riesgo, F. P. Guiomar, A. N. Sousa, A. L. Teixeira, N. J. Muga, M. C. R. Medeiros, and P. P. Monteiro, "200G outdoor free-space-optics link using a single-photodiode receiver," *J. Lightw. Technol.*, vol. 38, no. 2, pp. 394–400, 2020.
- [15] F. P. Guiomar, A. Lorences-Riesgo, D. Ranzal, F. Rocco, A. N. Sousa, M. A. Fernandes, B. T. Brandao, A. Carena, A. L. Teixeira, M. C. R. Medeiros, and P. P. Monteiro, "Adaptive probabilistic shaped modulation for high-capacity free-space optical links," *J. Lightw. Technol.*, vol. 38, no. 23, pp. 6529–6541, 2020.
- [16] K. Matsuda, M. Binkai, S. Koshikawa, T. Yoshida, H. Sano, Y. Konishi, and N. Suzuki, "Field demonstration of real-time 14 Tb/s 220 m FSO transmission with class 1 eye-safe 9-aperture transmitter," in *Optical Fiber Communications Conference and Exhibition (OFC)*, 2021, p. F3C.2.
- [17] H.-H. Lu, X.-H. Huang, W.-S. Tsai, C.-Y. Feng, C.-R. Chou, Y.-H. Chen, Y.-T. Huang, and A. Nainggolan, "800 Gb/s/200 m FSO link with a WDM-PAM4 scheme and SLM-based beam tracking technology," *Optics Letters*, vol. 46, no. 6, p. 1269, 2021.
- [18] M. Toyoshima, "Recent trends in space laser communications for small satellites and constellations," *J. Lightw. Technol.*, vol. 39, no. 3, pp. 693–699, feb 2021.
- [19] L. Paillier, R. L. Bidan, J.-M. Conan, G. Artaud, N. Vedrenne, and Y. Jaouen, "Space-ground coherent optical links: Ground receiver performance with adaptive optics and digital phase-locked loop," *J. Lightw. Technol.*, vol. 38, no. 20, pp. 5716–5727, oct 2020.
- [20] H. Kaushal and G. Kaddoum, "Optical communication in space: Challenges and mitigation techniques," *IEEE Commun. Surveys Tuts.*, vol. 19, no. 1, pp. 57–96, 2017.
- [21] A. S. Hamza, J. S. Deogun, and D. R. Alexander, "Wireless communication in data centers: A survey," *IEEE Commun. Surveys Tuts.*, vol. 18, no. 3, pp. 1572–1595, 2016.
- [22] W. Ali, G. Cossu, L. Gilli, E. Ertunc, A. Messa, A. Sturmiolo, and E. Ciaramella, "10 Gbit/s OWC system for intra-data centers links," *IEEE Photon. Technol. Lett.*, vol. 31, no. 11, pp. 805–808, jun 2019.
- [23] A. AlGhadhban, A. Celik, B. Shihada, and M.-S. Alouini, "LightFDG: An integrated approach to flow detection and grooming in optical wireless DCNs," *IEEE Trans. Netw. Service Manag.*, vol. 17, no. 2, pp. 1153–1166, jun 2020.
- [24] A. Celik, A. AlGhadhban, B. Shihada, and M.-S. Alouini, "Design and provision of traffic grooming for optical wireless data center networks," *IEEE Trans. Commun.*, vol. 67, no. 3, pp. 2245–2259, mar 2019.
- [25] ECSYSTEM, "Full duplex 10 Gbps FSO system," ECSYSTEM, Tech. Rep., 2021. [Online]. Available: <http://www.eurocro.cz/en/products/free-space-optics>
- [26] P. T. Dat, A. Bekkali, K. Kazaura, K. Wakamori, and M. Matsumoto, "A universal platform for ubiquitous wireless communications using radio over FSO system," *J. Lightw. Technol.*, vol. 28, pp. 2258–2267, 2010.
- [27] F. P. Guiomar, M. A. Fernandes, J. L. Nascimento, and P. P. Monteiro, "400G+ wireless transmission via free-space optics," in *2021 European Conference on Optical Communication (ECOC)*, 2021.
- [28] M. A. Fernandes, P. P. Monteiro, and F. P. Guiomar, "Single-wavelength Terabit FSO channel for datacenter interconnects enabled by adaptive PCS," in *Optical Fiber Communications Conference and Exhibition (OFC)*, 2021, p. Th5E.3.
- [29] —, "Free-space Terabit optical interconnects," *J. Lightw. Technol.*, vol. 40, no. 5, pp. 1519–1526, mar 2022.
- [30] C. Schieler, B. S. Robinson, O. Guldner, B. Bilyeu, A. S. Garg, K. Riesing, J. T. Chang, and F. Hakimi, "NASA's terabyte infrared delivery (TBIRD) program: Large-volume data transfer from LEO," in *33rd Annual AIAA/USU Conference on Small Satellites*, 2019, pp. SSC19–VI–02.
- [31] L. Jiang, T. Dai, X. Yu, Z. Dai, C. Wang, and S. Tong, "Analysis of scintillation effects along a 7 km urban space laser communication path," *Applied Optics*, vol. 59, no. 27, p. 8418, sep 2020.
- [32] I. S. Ansari, F. Yilmaz, and M. Alouini, "Performance analysis of free-space optical links over Málaga (\mathcal{M}) turbulence channels with pointing errors," *IEEE Trans. Wireless Commun.*, vol. 15, no. 1, pp. 91–102, Jan. 2016.
- [33] A. A. Farid and S. Hranilovic, "Outage capacity optimization for free-space optical links with pointing errors," *J. Lightw. Technol.*, vol. 25, no. 7, pp. 1702–1710, Jul. 2007.

- [34] E. Saleh Altubaishi and K. Alhamawi, "Capacity analysis of hybrid AF multi-hop FSO/RF system under pointing errors and weather effects," *IEEE Photon. Technol. Lett.*, vol. 31, no. 15, pp. 1304–1307, Aug. 2019.
- [35] R. S. Lawrence and J. W. Strohbehn, "A survey of clear-air propagation effects relevant to optical communications," *Proc. IEEE*, vol. 58, no. 10, pp. 1523–1545, Oct. 1970.
- [36] J. H. Churnside and S. F. Clifford, "Log-normal Rician probability-density function of optical scintillations in the turbulent atmosphere," *J. Opt. Soc. Am. A*, vol. 4, no. 10, pp. 1923–1930, Oct 1987.
- [37] A. Al-Habash, L. C. Andrews, and R. L. Phillips, "Mathematical model for the irradiance probability density function of a laser beam propagating through turbulent media," *Optical Engineering*, vol. 40, no. 8, pp. 1554 – 1562, 2001.
- [38] A. Ishimaru, "Theory and application of wave propagation and scattering in random media," *Proc. IEEE*, vol. 65, no. 7, pp. 1030–1061, Jul. 1977.
- [39] A. Mostafa and S. Hranilovic, "Channel measurement and Markov modeling of an urban free-space optical link," *IEEE J. Opt. Commun. Netw.*, vol. 4, no. 10, pp. 836–846, Oct. 2012.
- [40] S. Song, Y. Liu, T. Xu, S. Liao, and L. Guo, "Channel prediction for intelligent FSO transmission system," *Opt. Express*, vol. 29, no. 17, p. 27882, aug 2021.
- [41] M. A. Esmail, W. S. Saif, A. M. Ragheb, and S. A. Alshebeili, "Free space optic channel monitoring using machine learning," *Opt. Express*, vol. 29, no. 7, p. 10967, mar 2021.
- [42] M. A. Fernandes, P. P. Monteiro, and F. P. Guiomar, "Highly reliable outdoor 400G FSO transmission enabled by ANN channel estimation," in *Proc. Optical Fiber Conference (OFC)*, 2022, p. W31.4.
- [43] Y. Kaymak, R. Rojas-Cessa, J. Feng, N. Ansari, M. Zhou, and T. Zhang, "A survey on acquisition, tracking, and pointing mechanisms for mobile free-space optical communications," *IEEE Commun. Surveys Tuts.*, vol. 20, no. 2, pp. 1104–1123, 2018.
- [44] M. Fernandes, B. Brandão, P. Georgieva, P. Monteiro, and F. Guiomar, "Adaptive optical beam alignment and link protection switching for 5G-over-FSO," *Opt. Express*, may 2021.
- [45] X. Wang, X. Su, G. Liu, J. Han, W. Zhu, and Z. Liu, "Method to improve the detection accuracy of quadrant detector based on neural network," *IEEE Photon. Technol. Lett.*, vol. 33, no. 22, pp. 1254–1257, nov 2021.
- [46] M. M. Abadi, M. A. Cox, R. E. Alsaigh, S. Viola, A. Forbes, and M. P. J. Lavery, "A space division multiplexed free-space-optical communication system that can auto-locate and fully self align with a remote transceiver," *Scientific Reports*, vol. 9, no. 1, dec 2019.
- [47] R. Singh, F. Feng, Y. Hong, G. Faulkner, R. Deshmukh, G. Vercasson, O. Bouchet, P. Petropoulos, and D. O'Brien, "Design and characterisation of Terabit/s capable compact localisation and beam-steering terminals for fiber-wireless-fiber links," *J. Lightw. Technol.*, vol. 38, no. 24, pp. 6817–6826, dec 2020.
- [48] F. P. Guiomar, M. A. Fernandes, J. L. Nascimento, and P. P. Monteiro. (2022) 800G Coherent FSO Demonstration: Datasets and Post-Processing Routines. [Online]. Available: <https://doi.org/10.5281/zenodo.5819082>
- [49] T. Umezawa, S. Nakajima, A. Kanno, and N. Yamamoto, "Submillimeter large high-speed photodetector for high optical alignment robustness optical wireless communications," in *2021 European Conference on Optical Communication (ECOC)*, sep 2021, p. Th1B.5.
- [50] T. Koonen, K. Mekonnen, F. Huijskens, N. Q. Pham, Z. Cao, and E. Tangdiongga, "Optical wireless GbE receiver with large field-of-view," in *European Conference on Optical Communication (ECOC)*, sep. 2021, p. Th1B.6.
- [51] E. Ciaramella, Y. Arimoto, G. Contestabile, M. Presi, A. D'Errico, V. Guarino, and M. Matsumoto, "1.28-Tb/s (32 × 40 Gb/s) free-space optical WDM transmission system," *IEEE Photon. Technol. Lett.*, vol. 21, no. 16, pp. 1121–1123, Aug. 2009.
- [52] N. Fontaine, R. Ryf, Y. Zhang, J. Alvarado-Zacarias, S. van der Heide, M. Mazur, H. Huang, H. Chen, R. Amezcua-Correa, G. Li, M. Capuzzo, M. Kopf, A. Tate, H. Safar, C. Bolle, D. Neilson, E. Burrows, K. Kim, M. Bigot-Astruc, F. Achten, P. Sillard, A. Amezcua-Correa, and J. Carpenter, "Digital turbulence compensation of free space optical link with multimode optical amplifier," in *45th European Conference on Optical Communication (ECOC)*, 2019.
- [53] B. Zhang, R. Yuan, J. Sun, J. Cheng, and M.-S. Alouini, "Free-space optical communication using non-mode-selective photonic lantern-based coherent receiver," *IEEE Trans. Commun.*, vol. 69, no. 8, pp. 5367–5380, aug 2021.
- [54] V. Billault, J. Bourderionnet, J. P. Mazellier, L. Leviandier, P. Feneyrou, A. Maho, M. Sotom, X. Normandin, H. Lonjaret, and A. Brignon, "Free space optical communication receiver based on a spatial demultiplexer and a photonic integrated coherent combining circuit," *Opt. Express*, vol. 29, no. 21, p. 33134, sep 2021.
- [55] Thorlabs. (2021) ZST200 series stepper motor actuators. [Online]. Available: <https://www.thorlabs.com/thorproduct.cfm?partnumber=ZST206>
- [56] R. B. Stull, Ed., *An Introduction to Boundary Layer Meteorology*. Springer Netherlands, 1988.
- [57] L. C. Andrews, R. L. Phillips, and C. Y. Young, *Laser Beam Scintillation with Applications*. SPIE, jul 2001.
- [58] H. Sun, M. Torbatian, M. Karimi, R. Maher, S. Thomson, M. Tehrani, Y. Gao, A. Kumpera, G. Soliman, A. Kakkar, M. Osman, Z. A. El-Sahn, C. Daggart, W. Hou, S. Sutarwala, Y. Wu, M. R. Chitgarha, V. Lal, H.-S. Tsai, S. Corzine, J. Zhang, J. Osenbach, S. Buggaveeti, Z. Morbi, M. I. Olmedo, I. Leung, X. Xu, P. Samra, V. Dominic, S. Sanders, M. Ziari, A. Napoli, B. Spinnler, K.-T. Wu, and P. Kandappan, "800G DSP ASIC design using probabilistic shaping and digital sub-carrier multiplexing," *J. Lightw. Technol.*, vol. 38, no. 17, pp. 4744–4756.
- [59] Optical Internetworking Forum. 800G coherent project. [Online]. Available: <https://www.oiforum.com/technical-work/hot-topics/800g-coherent/>
- [60] G. Böcherer, P. Schulte, and F. Steiner, "Probabilistic shaping and forward error correction for fiber-optic communication systems," *J. Lightw. Technol.*, vol. 37, no. 2, pp. 230–244, Jan. 2019.
- [61] F. R. Kschischang and S. Pasupathy, "Optimal nonuniform signaling for Gaussian channels," *IEEE Trans. Inf. Theory*, vol. 39, no. 3, pp. 913–929, May 1993.
- [62] P. Schulte and G. Böcherer, "Constant composition distribution matching," *IEEE Trans. Inf. Theory*, vol. 62, no. 1, pp. 430–434, Jan 2016.
- [63] I. Fatadin, S. J. Savory, and D. Ives, "Compensation of quadrature imbalance in an optical QPSK coherent receiver," *IEEE Photon. Technol. Lett.*, vol. 20, no. 20, pp. 1733–1735, 2008.
- [64] M. Paskov, D. Lavery, and S. Savory, "Blind equalization of receiver in-phase/quadrature skew in the presence of Nyquist filtering," *IEEE Photon. Technol. Lett.*, vol. 25, no. 24, pp. 2446–2449, 2013.
- [65] F. P. Guiomar, S. B. Amado, A. Carena, G. Bosco, A. Nespolo, A. L. Teixeira, and A. N. Pinto, "Fully-blind linear and nonlinear equalization for 100G PM-64QAM optical systems," *J. Lightw. Technol.*, vol. 33, no. 7, pp. 1265–1274, 2015.
- [66] D. Rife and R. Boorstyn, "Single tone parameter estimation from discrete-time observations," *IEEE Trans. Inf. Theory*, vol. 20, no. 5, pp. 591–598, Sep 1974.
- [67] M. Magarini, L. Barletta, A. Spalvieri, F. Vacondio, T. Pfau, M. Pepe, M. Bertolini, and G. Gavioli, "Pilot-symbols-aided carrier-phase recovery for 100-G PM-QPSK digital coherent receivers," *IEEE Photon. Technol. Lett.*, vol. 24, no. 9, pp. 739–741, may1, 2012.
- [68] M. Faruk and K. Kikuchi, "Compensation for in-phase/quadrature imbalance in coherent-receiver front end for optical quadrature amplitude modulation," *IEEE Photon. J.*, vol. 5, no. 2, pp. 7800 110–7800 110, 2013.
- [69] A. Alvarado, E. Agrell, D. Lavery, R. Maher, and P. Bayvel, "Replacing the soft-decision FEC limit paradigm in the design of optical communication systems," *J. Lightw. Technol.*, vol. 33, no. 20, pp. 4338–4352, Oct 2015.
- [70] A. Alvarado, T. Fehenberger, B. Chen, and F. M. J. Willems, "Achievable information rates for fiber optics: Applications and computations," *J. Lightw. Technol.*, vol. 36, no. 2, pp. 424–439, Jan. 2018.
- [71] Portuguese Institute for Sea and Atmosphere. (2021) Interface de programação de aplicações do IPMA. [Online]. Available: <https://api.ipma.pt/>
- [72] M. Abtahi, P. Lemieux, W. Mathlouthi, and L. A. Rusch, "Suppression of turbulence-induced scintillation in free-space optical communication systems using saturated optical amplifiers," *J. Lightw. Technol.*, vol. 24, no. 12, pp. 4966–4973, dec 2006.
- [73] K. Yiannopoulos, N. C. Sagias, and A. C. Boucouvalas, "On the performance of semiconductor optical amplifier-assisted outdoor optical wireless links," *IEEE J. Sel. Areas Commun.*, vol. 33, no. 9, pp. 1869–1876, Sep. 2015.
- [74] Y.-Q. Hong and S.-K. Han, "Polarization-dependent SOA-based PolSK modulation for turbulence-robust FSO communication," *Opt. Express*, vol. 29, no. 10, p. 15587, may 2021.